Loss of *Elp1* in cerebellar granule cell progenitors models ataxia phenotype of Familial Dysautonomia

Frederik Arnskötter [a,b,c,d], Patricia Benites Goncalves da Silva [a,b,c], Mackenna E. Schouw [a,b,c], Chiara Lukasch [a,b,c], Luca Bianchini [a,b,c,d], Laura Sieber [a,b,c], Jesus Garcia-Lopez [e,f,g], Shiekh Tanveer Ahmad [e,f], Yiran Li [e,f], Hong Lin [e,f], Piyush Joshi [a,b,c], Lisa Spänig [a,b,c,d], Magdalena Radoš [a,b,c], Mykola Roiuk [h], Mari Sepp [i], Marc Zuckermann [b,c,j], Paul A. Northcott [e,f], Annarita Patrizi [k], Lena M. Kutscher [a,b,c,*]

[a] *Developmental Origins of Pediatric Cancer Junior Research Group, German Cancer Research Center (DKFZ), Heidelberg, Germany*
[b] *Hopp Children's Cancer Center (KiTZ), Heidelberg, Germany*
[c] *National Center for Tumor Diseases (NCT), NCT Heidelberg, A partnership between DKFZ and Heidelberg University Hospital, Germany*
[d] *Faculty of Biosciences, Heidelberg University, Heidelberg, Germany*
[e] *Department of Developmental Neurobiology, St. Jude Children's Research Hospital, Memphis, TN, USA*
[f] *Center of Excellence in Neuro-Oncology Sciences (CENOS), St. Jude Children's Research Hospital, Memphis, TN, USA*
[g] *Department of In vivo Pharmacology-Immunology, Tempest Therapeutics, Brisbane, CA, USA*
[h] *Signal Transduction in Cancer and Metabolism, German Cancer Research Center (DKFZ), Heidelberg, Germany*
[i] *Center for Molecular Biology of Heidelberg University (ZMBH), DKFZ-ZMBH Alliance, Heidelberg, Germany*
[j] *Division of Pediatric Neuro-Oncology, Preclinical Modeling Group, German Cancer Research Center (DKFZ), Heidelberg, Germany*
[k] *Schaller Research Group, German Cancer Research Center (DKFZ), Heidelberg, Germany*

ARTICLE INFO

ABSTRACT

Familial Dysautonomia (FD) is an autosomal recessive disorder caused by a splice site mutation in the gene *ELP1*, which disproportionally affects neurons. While classically characterized by deficits in sensory and autonomic neurons, neuronal defects in the central nervous system have also been described. Although *ELP1* expression remains high in the normal developing and adult cerebellum, its role in cerebellar development is unknown. To explore the role of *Elp1* in the cerebellum, we knocked out *Elp1* in cerebellar granule cell progenitors (GCPs) and examined the outcome on animal behavior and cellular composition. We found that GCP-specific conditional knockout of *Elp1* (*Elp1*^cKO) resulted in ataxia by 8 weeks of age. Cellular characterization showed that the animals had smaller cerebella with fewer granule cells. This defect was already apparent as early as 7 days after birth, when *Elp1*^cKO animals also had fewer mitotic GCPs and shorter Purkinje dendrites. Through molecular characterization, we found that loss of *Elp1* was associated with an increase in apoptotic cell death and cell stress pathways in GCPs. Our study demonstrates the importance of *ELP1* in the developing cerebellum, and suggests that loss of *Elp1* in the GC lineage may also play a role in the progressive ataxia phenotypes of FD patients.

1. Introduction

Familial Dysautonomia (FD; OMIM: 223900), also known as Riley-Day syndrome or hereditary sensory and autonomic neuropathy type III (HSAN III), is an autosomal-recessive degenerative disorder of the sensory and autonomic nervous systems (Rotthier et al., 2012).

Neuronal deficits in the central nervous system have also been reported (Gutiérrez et al., 2015; Mendoza-Santiesteban et al., 2012). Hallmark symptoms of FD include insensitivity to temperature and pain, inability to cry, cardiovascular instability, retinal degeneration and progressive ataxia (González-Duarte et al., 2023; Rotthier et al., 2012); only 50% of patients reach the age of 40 (Axelrod et al., 2002). Genetically, FD is

---

caused by a homozygous splice site mutation in *ELP1* (Anderson et al. (2001); OMIM: 603722), resulting in tissue-specific skipping of exon 20 and severely reduced ELP1 protein levels (Slaugenhaupt et al., 2001), especially in neurons (Cuajungco et al., 2003). *ELP1* encodes the scaffolding subunit of the highly conserved multi-subunit Elongator complex, which modifies specific tRNAs with 5-carboxymethyl derivatives (xcm^5) to ensure anticodon-codon pairing and effective protein translation (Abbassi et al., 2024; Karlsborn et al., 2014).

The cerebellum primarily coordinates motor function and balance, and cerebellar dysfunction is often associated with progressive ataxias (Schmahmann, 2019). In FD patients, *ELP1* is preferentially mis-spliced in the cerebellum compared with other organs (Hims et al., 2007), suggesting that ELP1 protein levels may also be decreased in the cerebellum of FD patients. Among healthy tissues, *ELP1* gene expression is the highest in the cerebellum compared with other brain regions and organs in humans (Anderson et al., 2001; Waszak et al., 2020). However, the role of *ELP1* in the cerebellum and how its loss may contribute to ataxia remains unexplored.

To investigate the function of *Elp1* in the cerebellum and determine whether loss of *Elp1* may contribute to ataxia, we used an *Atoh1-Cre* driven conditional knockout approach to eliminate *Elp1* in developing granule cell progenitor (GCP) cells (*Elp1^cKO^*). *Elp1^cKO^* animals developed ataxia by 8 weeks of age. While the overall cytoarchitecture of the *Elp1^cKO^* cerebellum was unaffected, *Elp1^cKO^* animals had fewer GCs at 4 and 12 weeks of age, resulting in smaller cerebella compared with littermate controls. At postnatal day 7 (P7), *Elp1^cKO^* animals had fewer mature GCs, decreased expression of the glutamatergic transporter VGluT1, and shorter Purkinje dendrites. These cellular phenotypes were likely the direct result of increased apoptosis at P7. Our study suggests that *Elp1* loss in the GC lineage may contribute to the ataxic symptoms observed in FD patients.

2. Materials and methods

2.1. Animals

Elp1 floxed mice were generated by breeding *Elp1* knockout first animals (*Elp1*^tm1a(KOMP)Wtsi^; *Elp1-LacZ*, George et al. (2013)) to ubiquitous *Flp* expressing mice (Rodríguez et al. (2000); JAX, #005703). To generate *Elp1* conditional knockout mice, *Elp1^fl/fl^* animals were crossed with *Atoh1-Cre* (Matei et al. (2005); JAX, #011104). Genotyping primer sequences available in Supplemental Table S1. Mice were bred on a C57BL/6N background. Animals were housed in a temperature-controlled vivarium on a 12 h:12 h light-dark cycle with *ad libitum* food and water. Animals of both sexes were used for experiments. Cre-positive, homozygous *Elp1^fl/fl^* (*Elp1^cKO^*) were used as experimental mice, while Cre-negative littermates (*Elp1^fl/+^* or *Elp1^fl/fl^*) were used as controls. All animal experiments for this study were conducted according to the animal welfare regulations approved by the responsible authorities in Baden-Württemberg, Germany (Regierungspraesidium Karlsruhe, approval numbers: G-172/18, G-136/23).

2.1.1. Motor behavior studies

Motor behavior studies were performed at the Interdisciplinary Neurobehavioral Core (INBC) at the University of Heidelberg. Data collection was performed by the same experimenter blinded to genotype. Experiments were carried out during the light phase. Animals were acclimated to the test room for at least 1–2 days before testing. Weight measurements, rotarod, grip strength, and CatWalk tests were performed at 8, 10, and 12 weeks of age.

2.1.2. SHIRPA, rotarod, grip strength assay

To assess overall animal health, we performed a modified SHIRPA primary screen (Rogers et al., 1997), including examination of spontaneous activity, body position, body tone, visual placing, hind limb splay, catalepsy, negative geotaxis, and several reflexes at week 7. Examined

tests, procedures and scoring schemes are shown in Supplemental Table S2. Rotarod and grip strength tests were performed as described in Eltokhi et al. (2021). Briefly, we used an accelerating Rotarod system, and tested animals for a maximum of 8 min. Animals completed 3 trials per day with a break (10 min) between the trials, and measurements were averaged. For the grip strength assay, animals pulled on a fixed stirrup, and the strength of the front paw was measured three times; measurements were averaged. Rotarod and grip strength raw data is available as Supplemental Table S3.

2.1.3. CatWalk gait analysis

For gait analysis, a digital CatWalk was used (CatWalk XT, Noldus Information Technology BV, Hamers et al. (2006)). Animals were placed at one end of a 130-cm tube, and the parameters were automatically calculated. Animals were tested three times per time point and measurements were averaged. Due to differences in body weight, female and male mice were analyzed separately. Raw data is available in Supplemental Tables S4 and S5.

2.1.4. EdU injections

P7 mice of the appropriate genotype were injected intraperitoneally with 10 mg/ml stock solution of EdU (50 mg/kg, 20 μl total volume, dissolved in PBS, Invitrogen). Mice were sacrificed at 2 h post-injection. Brains were harvested, fixed overnight in 4% paraformaldehyde (PFA) at 4 °C, soaked in 30% sucrose in PBS overnight, and embedded in Optimal Cutting Temperature (OCT) compound. Frozen 10 μm-thick sections were collected on Fisher Superfrost Plus slides using a cryostat and treated with Click-iT™ EdU imaging reagent (Invitrogen).

2.1.5. Tissue preparation, immunofluorescence staining, and quantification

Adult mice were anaesthetized with a ketamine/xylazine/acepromazine mix and transcardially perfused with 4% PFA in phosphate-buffered saline (PBS, pH 7.4). After, brains were harvested, post-fixed in 4% PFA at 4 °C, soaked in 30% sucrose in PBS overnight, and embedded in OCT compound. Immunofluorescence staining was performed as previously described (Kutscher et al., 2020). Antibodies used are listed in Supplemental Table S1. All slides were counterstained with DAPI (300 nM). Imaging and quantification were performed blinded to genotype. For display, comparative immunostainings were edited with identical settings including rolling ball background subtraction in FIJI (Schindelin et al., 2012). For display of cerebellum overview images, the cerebellum was segmented on black background. For quantification, the number of average positive cells was counted using FIJI's cell counter plugin in 3–4100 μm × 100 μm regions in at least 3 independent cerebella in the same lobule and region, as indicated in the figures. During initial analyses, multiple lobules were quantified. Because the results were robust across lobes, representative lobules were quantified in later experiments, as indicated in figure legends. For quantification of the area, mean intensity, or nuclei number from whole cerebellum images, the layers were manually segmented and measured in FIJI. The number of nuclei was determined using the semi-automatic thresholding/ watershed/find particle (P7/28) or find maxima (12 weeks) workflows in FIJI.

2.2. GCP isolation, culture and proliferation assay

GCP isolation was performed as previously described (Hatten, 1985; Kawauchi et al., 2012) and cell density was diluted to 2.5×10^6 cells/ml with GCP media. For *in vitro* studies, GCPs were plated on 6-well (2 ml, immunoblot) and 24-well plates (0.4 ml; qPCR or EdU proliferation assay) for 72 h in the presence or absence of 200 nM Smoothened agonist (Merck). Full medium changes were performed daily. Cell proliferation assay was performed as described in Haag et al. (2021). Briefly, a final concentration of 10 μM EdU was added to the culture medium and incubated for 1 h. Proliferative cells were labeled using the Click-iT EdU Alexa Fluor 647 Flow Cytometry Assay Kit (Life Technologies) according

to manufacturer's instruction.

2.3. Quantitative PCR (qPCR)

RNA was extracted with the Maxwell® RSC simplyRNA tissue kit (Promega) and cDNA was generated with SuperScript II kit (Invitrogen). qPCR was performed with SYBR green PCR master mix (Applied Biosystems) with 10 ng cDNA input in triplicates on a QuantStudio 5 real-time PCR system (Thermo Fisher Scientific). Primer sequences are listed in Supplemental Table S1. Relative gene expression was compared to reference gene *Tbp1*.

2.4. RNA extraction and RNA-seq analysis

Tissue was homogenized using a QIAshredder (Qiagen). RNA was extracted with RNeasy Mini Plus Kit (Qiagen) following supplier's instructions. For measurement of RNA quantity, ND1000 Spectrophotometer (NanoDrop Technologies) and/or Agilent 2100 Bioanalyzer was used.

Paired-end sequencing was performed on a NovaSeq 6000 (Illumina). FastQC-v0.11.8 was used for quality control of RNA-seq reads. BBDuk (minlen = 30; others default) was used to remove remaining adapters and low-quality bases. The alignment of raw FASTQs was performed using STAR v2.5.3a tool (Dobin et al., 2013) to mouse reference genome (mm10). Count matrices were analyzed for differentially expressed genes with R package DESeq2 (Love et al., 2014). GSEA was performed with the R package clusterProfiler (v4.6; Wu et al. (2021)) based on the gene ontology biological processes gene set from MSigDB (v7.4.1) with a $p_{adj} < 0$ (Liberzon et al., 2011; Subramanian et al., 2005). GSEA results were visualized in Cytoscape with network edges defined by Jaccard distance between gene set pairs.

2.5. Analysis of snRNA-seq data

To profile *ELP1/Elp1* expression in cerebellar cell types, we used processed snRNA-seq data covering cerebellum development in human and mouse (Sepp et al., 2024) as available at https://apps.kaessmannlab.org/sc-cerebellum-transcriptome/. The data was filtered for the main cerebellar cell types (VZ_neuroblast, parabrachial, GABA_DN, Purkinje, interneuron, NTZ_neuroblast, glut_DN, isth_N, GC/UBC, GC, UBC, astroglia, oligo, ependymal, meningeal, immune), and grouped by biological replicate and cell type, requiring at least 50 cells per group. For deeper analysis of *Elp1* expression in the adult murine cerebellum, the published single-cell RNA-seq atlas from Kozareva et al. (2021) with its original identifiers was used. Two values were calculated for each group: fraction of cells positive (n[UMI] ≥1) for *ELP1* and mean expression per cell (*ELP1* n[UMI] / total n[UMI]). These values were then standardized separately for the data produced with the two Chromium versions (v2 and v3; 10x Genomics), using version-specific means and standard deviations calculated based on values averaged across the developmental stages and cell types that were covered by both Chromium versions. The obtained z-scored data were averaged across groups for presentation; in case of the cell fraction the values were back-transformed using the mean and standard deviation values averaged across the versions. Spatial transcriptomics data of the adult mouse cerebellum was taken from the published Slide-seq atlas by Langlieb et al. (2023; available at https://www.braincelldata.org/).

2.6. Protein extraction and immunoblotting

Protein extraction and immunoblotting was performed as described in Haag et al. (2021). Membranes were stripped and reprobed. Antibodies and reagents are listed in Supplemental Table S1.

2.7. Protein digestion and Tandem-Mass-Tag (TMT) labeling

The analysis was performed with a previously optimized protocol (Bai et al., 2017; Pagala et al., 2015). For whole proteome profiling, quantified protein samples (300 μg in the lysis buffer with 8 M urea) for each TMT channel were proteolyzed with Lys-C (Wako, 1:100 *w/w*) at 21 °C for 2 h, diluted by 4-fold to reduce urea to 2 M for the addition of trypsin (Promega, 1:50 w/w) to continue the digestion at 21 °C overnight. The insoluble debris was kept in the lysates for the recovery of insoluble proteins. The digestion was terminated by the addition of 1% trifluoroacetic acid. After centrifugation, the supernatant was desalted with the Sep-Pak C18 cartridge (Waters), and then dried by Speedvac (Thermo Fisher). Each sample was resuspended in 50 mM HEPES (pH 8.5) for TMT labeling and then mixed equally, followed by desalting for the subsequent fractionation. 0.1 mg protein per sample was used.

2.7.1. Extensive two-dimensional liquid chromatography-Tandem mass spectrometry (LC/LC-MS/MS)

The TMT labeled samples were fractionated by offline basic pH reverse phase LC, and each of these fractions was analyzed by the acidic pH reverse phase LC-MS/MS (Wang et al., 2014; Xu et al., 2009). We performed a 160 min offline LC run at a flow rate of 400 μl per minute on an XBridge C18 column (3.5 μm particle size, 4.6 mm × 25 cm, Waters; buffer A: 10 mM ammonium formate, pH 8.0; buffer B: 95% acetonitrile, 10 mM ammonium formate, pH 8.0; Bai et al. (2017)). A total of 80 two-min fractions was collected. Every forty-first fraction was concatenated into 40 pooled fractions which were subsequently used for whole proteome TMT analysis.

In the acidic pH LC-MS/MS analysis, each fraction from basic pH LC was dried by a Speedvac and was run sequentially on a column (75 μm × 35 cm for the whole proteome, 50 μm × 30 cm for whole proteome, 1.9 μm C18 resin from Dr. Maisch GmbH, 65 °C to reduce backpressure) interfaced with a Fusion MS (Thermo Fisher) for the whole proteome where peptides were eluted by a 90 min gradient (buffer A: 0.2% formic acid, 5% DMSO; buffer B: buffer A plus 65% acetonitrile). MS settings included the MS1 scan (410–1600 *m/z*, 60,000 resolution, 1×10^6 AGC and 50 ms maximal ion time) and 20 data-dependent MS2 scans (fixed first mass of 120 m/z, 60,000 resolution, 1×10^5 AGC, 200 ms maximal ion time, HCD, 36% normalized collision energy, 1.0 m/z isolation window with 0.2 m/z offset, and 20 s dynamic exclusion). MS settings included the MS1 scan (450–1600 m/z, 60,000 resolution, 1×10^6 AGC and 50 ms maximal ion time) and 20 data-dependent MS2 scans (fixed first mass of 120 m/z, 60,000 resolution, 1×10^5 AGC, 110 ms maximal ion time, HCD, 36% normalized collision energy, 1.0 m/z isolation window with 0.2 m/z offset, and 10 s dynamic exclusion).

2.8. tRNA modification analysis

tRNA modification analysis was performed by Arraystar Inc. (Rockville, USA). Briefly, tRNAs were isolated from total RNA by Urea-PAGE electrophoresis. 60–90 nt tRNA bands were excised, purified by ethanol precipitation and quantified by Qubit RNA HS assay (Thermo Fisher). tRNAs were hydrolyzed to single nucleosides, dephosphorylated and deproteinized using 10.000-Da MWCO spin filter (Sartorius). Analysis of nucleoside mixtures was performed on Agilent 6460 QQQ mass spectrometer with an Agilent 1260 HPLC system. LC-MS data was acquired using Agilent Qualitative Analysis software. MRM peaks of each modified nucleoside were extracted and normalized to the sum of all modifications peak area.

2.9. Statistical analysis

Statistical analysis was performed with GraphPad Prism (version 10.2.0). Data was tested for normal distribution and parametric tests (unpaired *t*-test) were used only if the data was normally distributed. Otherwise, a nonparametric test such as Mann-Whitney *U* test was

chosen. Statistical significance between groups was considered when *P* values ≤0.05; significance levels are $P < 0.05$ (*), $P < 0.005$ (**), $P < 0.0005$ (***), and $P < 0.0001$ (****), if not otherwise indicated. The statistical test used for each analysis is listed in each figure legend. Data presentation, applied statistical tests, biological replicate number *N* and technical replicate number *n* are indicated in the figure legends.

3. Results

3.1. ELP1 is highly expressed in proliferating granule cell progenitors and protein levels are downregulated upon differentiation

Previous studies have shown that *ELP1* exhibits the highest expression in the postnatal cerebellum throughout the development of major organs in humans, and in mice its expression gradually increases postnatally in cells of the GC lineage (Waszak et al., 2020). To further understand *ELP1* expression patterns during human and mouse cerebellar development, we examined *ELP1* levels across developmental stages and cell types. Bulk RNA-sequencing data (Cardoso-Moreira et al., 2019) indicates a trend of increasing *ELP1* expression in the cerebellum postnatally in humans, whereas a decrease is observed in the mouse (Supplemental Fig. S1A, B); however, the murine cerebellum maintains the highest expression of *Elp1* compared with other organs in adult mice. To investigate gene expression at the single-cell level, we examined cell-type-specific expression using published single-nucleus RNA-sequencing atlases of the developing mouse and human cerebellum (Sepp et al., 2024). *ELP1/Elp1* is broadly expressed in most cell types during cerebellar development (Supplemental Fig. S1C, D). Similar to the bulk expression in the mouse, overall *Elp1* expression at the single-cell level decreased upon birth in the majority of cell types, but expression was still maintained into adulthood in many cell types, including the GC, interneuron, and glial lineages (Fig. 1A; Supplemental Fig. S1C). In humans, *ELP1* expression was maintained throughout development, or increased toward adulthood in the GC, interneuron and glial lineages (Fig. 1B; Supplemental Fig. S1D).

To examine adult murine cell types, we examined recent snRNAseq and spatial transcriptomic atlases of the adult mouse brain (Kozareva et al., 2021; Langlieb et al., 2023), observing widespread *Elp1* expression in most cell types including mature Purkinje cells (PC) and unipolar brush cells (UBC; Supplemental Fig. S1E, F). In addition, X-gal staining of adult *Elp1-LacZ* reporter mice (George et al., 2013) showed *lacZ* expression throughout the granular layer (GL) and high levels in the PCL (Supplemental Fig. S1G). Despite different developmental dynamics between species, *ELP1/Elp1* is broadly expressed in the mouse and human cerebellum overall; in granule cells, its expression is maintained from early embryonic stages to adulthood.

Given the high proportion of GCs in the postnatal cerebellum, the high level of *ELP1* expression in GCs, and potential link to ataxia in FD patients, we first investigated protein expression of ELP1 in the GC lineage of the normal developing murine cerebellum. During the first two postnatal weeks of mice, PCs secrete SHH and stimulate the proliferation of GCPs in the outermost part of the external granular layer (EGL; Fig. 1C, D; Consalez et al. (2021)). Once GCPs exit cell cycle, they migrate inward and differentiate into mature GCs, forming the internal granular layer (IGL). At P7, both EGL and IGL are present, allowing us to examine both proliferating GCPs and mature GCs. Therefore, we injected EdU into wild type P7 pups to mark actively cycling cells, and performed immunofluorescence staining against ELP1 and EdU on brains harvested 2 h after injection (Fig. 1E, F). We found that proliferating GCPs in the outer EGL expressed higher levels of ELP1 than differentiating GCPs in the inner EGL or mature GCs in the IGL (Fig. 1E, F).

To identify the role of ELP1 in proliferating GCPs, we first validated whether ELP1 expression correlates with cell cycle using an *in vitro* proliferation assay (Fig. 1G). Briefly, we isolated GCPs from P7 mice and examined their response to SHH pathway activation by exposure to Smoothened agonist (SAG) *in vitro*. SAG treatment maintains the proliferation of purified GCPs, whereas withdrawal terminates proliferation and induces differentiation after 72 h *in vitro* (Wechsler-Reya and Scott (1999); Supplemental Fig. S2A, B). As expected, proliferating (SAG-treated) GCPs expressed higher levels of SHH pathway genes *Ccnd2, Gli2, Mycn, Gli1, Ccnd1, Ptch1* and the hallmark GCP transcription factor *Atoh1* compared with differentiating (untreated) GCPs (Fig. 1H; Supplemental Fig. S2A, C). In contrast, *Elp1* gene expression remained unchanged in proliferating and differentiating GCPs (Fig. 1H); however, at the protein level, proliferating GCPs expressed higher levels of ELP1 than differentiated GCs (Fig. 1I, J; Supplemental Fig. S2D, E). Protein levels of ELP2, another component of the Elongator core complex, were also reduced upon differentiation, but not those of ELP3, the catalytic subunit of the Elongator complex (Fig. 1I; Supplemental Fig. S2F, G). Overall, ELP1 shows increased expression in proliferating GCPs, which prompted us to next investigate the consequences of *Elp1* loss in cerebellar GCPs.

3.2. Conditional Elp1 knockout reduces ELP1 and Elongator in GCPs

To investigate the functional relevance of *Elp1* during GC development, we used a genetically engineered mouse strain (George et al., 2013) to generate Cre-inducible excision of exon 4 of *Elp1* in *Atoh1*-positive GCPs (Fig. 2A; hereafter called *Elp1*[cKO]). Immunofluorescence staining confirmed a specific reduction of ELP1 in GCPs, but not in PCs in P7 *Elp1*[cKO] mice (Fig. 2B; Supplemental Fig. S3A). While ELP1 was absent from the EGL of the anterior and central lobules of the *Elp1*[cKO] cerebella, ELP1 was present in the nodular lobules IX and X, where *Atoh1-Cre* transgene activity is known to be markedly reduced (Pan et al., 2009). We confirmed loss of ELP1 protein in purified *Elp1*[cKO] GCPs compared with littermate control GCPs (Fig. 2C, D). *Elp1*[cKO] GCPs also showed reduced levels of ELP2 and ELP3 (Fig. 2C, E, F), indicating the destabilization and degradation of the core Elongator complex upon ELP1 loss (Fig. 2G; Xu et al. (2015)). Notably, *Elp1*^{fl/+}; *Atoh1-Cre/+* (*Elp1*[HET]) GCPs exhibited intermediate levels of ELP1, ELP2, and ELP3 expression when compared with *Elp1*[cKO] and *Elp1*[WT] GCPs (Supplemental Fig. S3B). Given that *Elp1* haploinsufficiency results in reduced Elongator complex levels and might evoke downstream defects in *Elp1*[HET] animals, we did not use *Elp1*[HET] mice as controls. Despite higher ELP1 expression in proliferating GCPs (Fig. 1I, J), *in vitro* proliferation was similar in *Elp1*[cKO] GCPs compared to sibling controls, as assessed by EdU incorporation and PCNA protein levels (Fig. 2H; Supplemental Fig. S3C); however, levels of the DNA replication protein MCM2 were slightly increased (Supplemental Fig. S3D). The response to SHH pathway stimulation was unchanged in *Elp1*[cKO] GCPs (Fig. 2I; Supplemental Fig. S3E); however, the total number of GCPs purified from *Elp1*[cKO] animals was reduced (Fig. 2J), suggesting a loss of viable GCPs in the *Elp1*[cKO] cerebellum. Consistent with fewer GCPs, ATOH1 protein was significantly reduced in purified GCPs from *Elp1*[cKO] mice (Fig. 2C; Supplemental Fig. S3F). In summary, loss of *Elp1* destabilized the Elongator complex in proliferating GCPs, allowing us to use this mouse model to examine the effect of *Elp1* loss on animal behavior.

3.3. Elp1[cKO] mice develop ataxia

In contrast to the embryonic lethality of systemic *Elp1* knockout (Chen et al., 2009; Dietrich et al., 2011), *Elp1*[cKO] mice survived to adulthood. By week 12, *Elp1*[cKO] mice had an insecure, unsteady gait, similar to other FD-specific mouse models (Dietrich et al., 2012; Morini et al., 2023; Morini et al., 2016). To assess ataxia onset and progression, we performed a tailored battery of behavioral tests to assess general animal health, muscle strength, balance, motor coordination and gait over time (Fig. 3A). Behavioral analysis was performed blinded to genotype and included both sexes. First, we determined the overall health of the *Elp1*[cKO] mice by a SHIRPA primary screen at week 7 (see Methods for details), followed by movement and strength assessments using a rotarod assay, grip strength assay, and gait analysis at weeks 8, 10 and
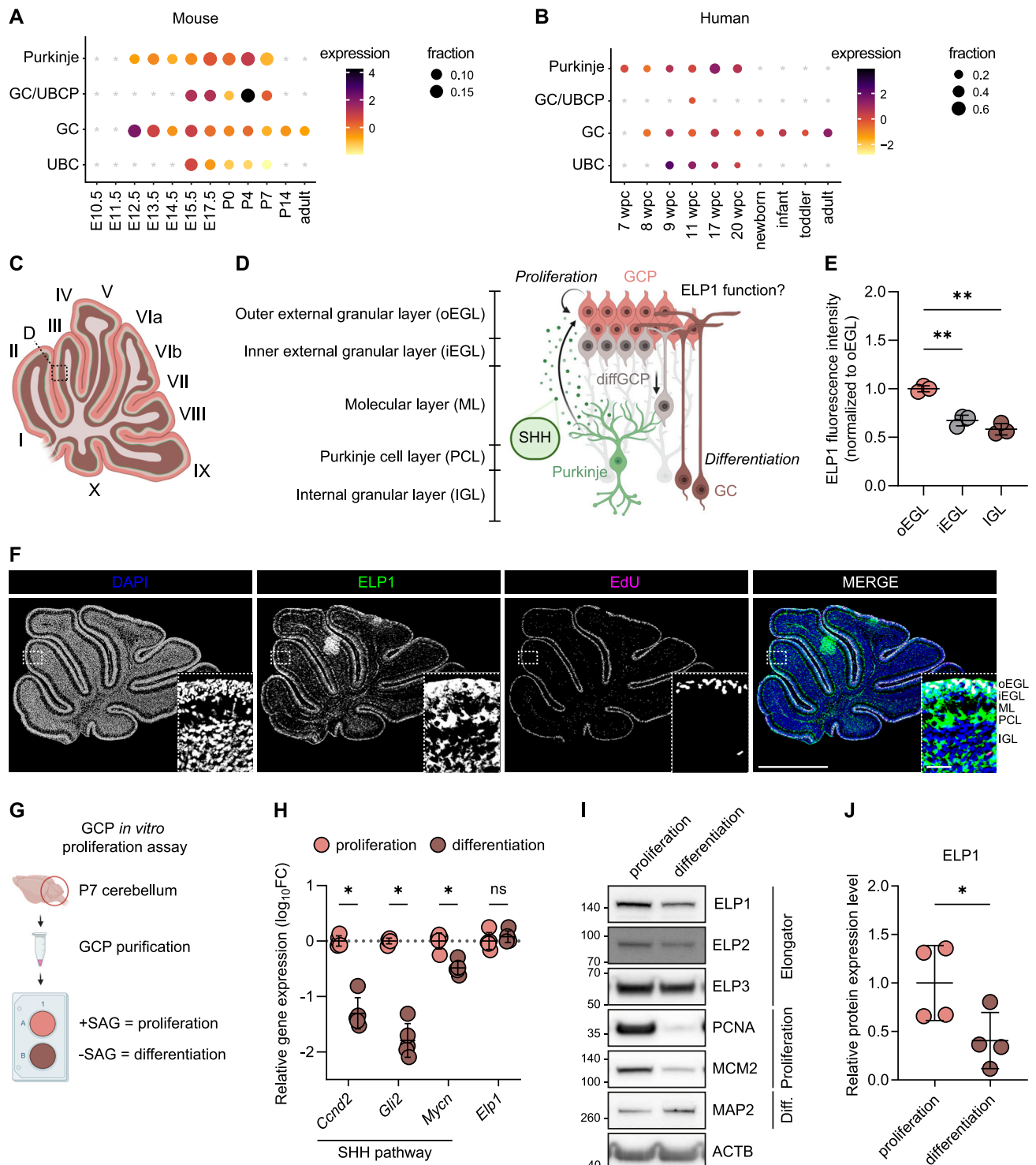
Fig. 1. ELP1 is expressed in proliferating granule cell progenitors during cerebellar development. (A-B) Expression of *Elp1/ELP1* in Purkinje and granule cell lineage cells at different time points of murine (A) and human (B) cerebellar development. Dot size and colour indicate fraction of cells and mean expression of *Elp1/ELP1*, respectively, averaged across biological replicates. Asterisks indicate missing data. Extended dot plot in Supplemental Fig. S1C,D. GC/UBCP, granule cell/unipolar brush cell progenitor. (C) Cartoon showing sagittal section of P7 murine cerebellum. (D) Cartoon showing layered cytoarchitecture and stages of GC lineage development in P7 mouse cerebellum. (E) Median ELP1 fluorescence intensity in the outer external granular layer (oEGL), inner external granular layer (iEGL), and internal granular layer (IGL) across lobules III, VI, IX and X. Paired *t*-tests. Mean ± SD. *N* = 3 mice, *n* = 4 lobules. (F) Representative immunofluorescence image of DAPI (blue), ELP1 (green) and EdU (magenta) in P7 *Elp1*^WT cerebellum. Scale bar, 1 mm. Inset, higher magnification of single z-slice of lobule III. Scale bar, 50 µm. ML, molecular layer. PCL, Purkinje cell layer. (G) Cartoon showing GCP *in vitro* proliferation assay. SAG, Smoothened agonist. (H) Relative mRNA expression (quantitative PCR) of *Ccnd2*, *Gli2*, *Mycn* and *Elp1* of GCPs cultured with SAG (orange, proliferation) or without SAG (brown, differentiation), normalized to *Tbp1*. Multiple Mann-Whitney *U* tests. *, $P < 0.005$. Mean ± SD. *N* = 5. SHH, Sonic hedgehog. (I) Immunoblot validation of ELP1, ELP2, ELP3, PCNA, MCM2, and MAP2 protein in GCPs cultured with SAG (proliferation) or without SAG (differentiation). ACTB was used as loading control. (J) Quantification of ELP1 protein abundance in P7 GCP lysates normalized to ACTB. Unpaired *t*-test. Mean ± SD. *N* = 4. (For interpretation of the references to colour in this figure legend, the reader is referred to the web version of this article.)
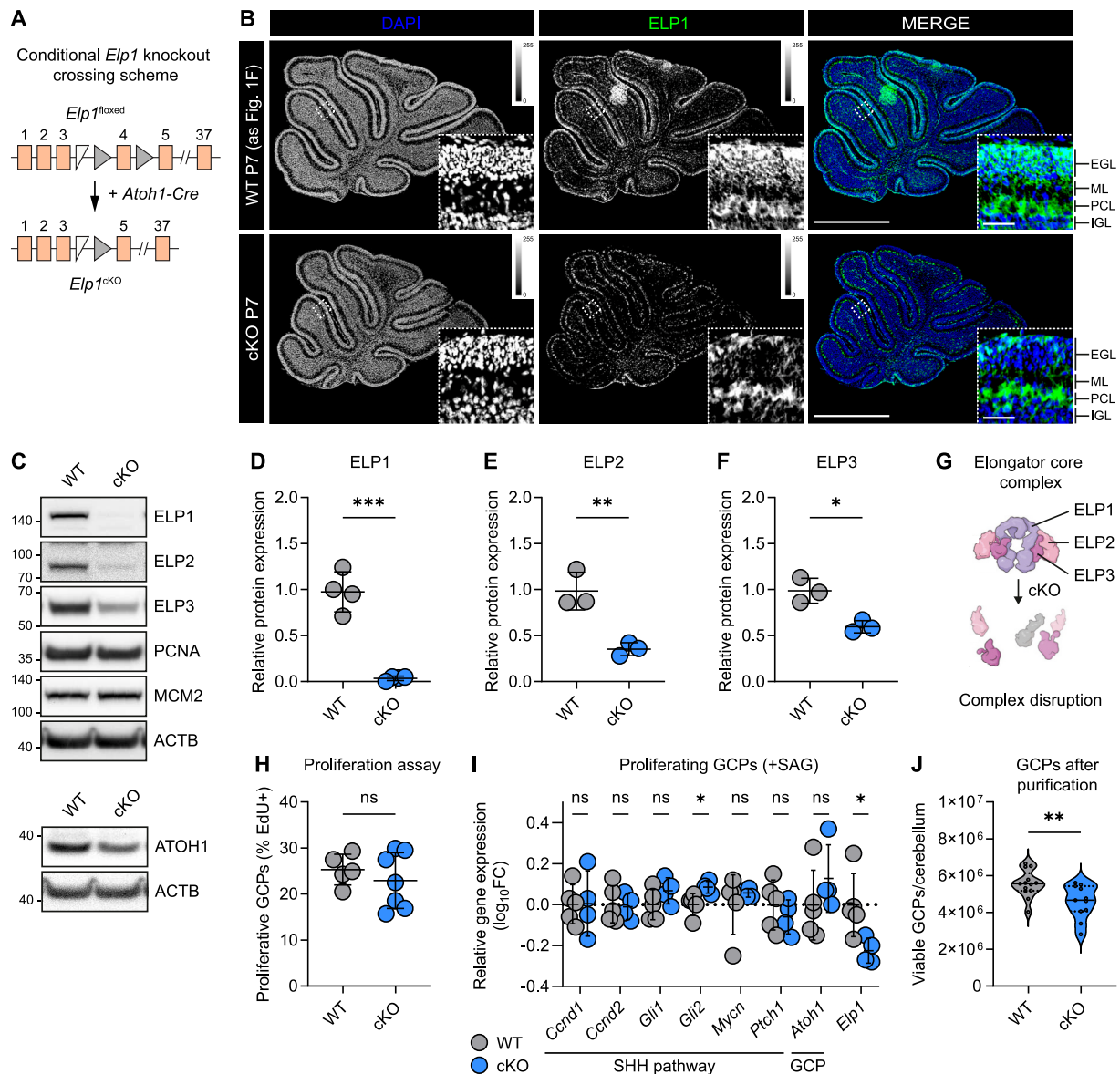
Fig. 2. GCP-specific *Elp1* knockout reduces ELP1 and destabilizes the Elongator core complex. (A) Schematic showing the crossing scheme of GCP-specific *Elp1* knockout, adapted from Chaverra et al. (2017). (B) Representative immunofluorescence images of DAPI (blue) and ELP1 (green) expression in P7 cerebella of *Elp1*[WT] (top row) and *Elp1*[cKO] (bottom row) littermates. *Elp1*[cKO] cerebellum is the same as in Fig. 1F. Single z-slice. Scale bar, 1 mm. Inset, magnification of lobule III. Scale bar, 50 μm. EGL, external granular layer. ML, molecular layer. PCL, Purkinje cell layer. IGL, internal granular layer. (C) Immunoblot validation of ELP1, ELP2, ELP3, PCNA, MCM2, and ATOH1 protein abundance in *Elp1*[cKO] and *Elp1*[WT] GCP lysates. ACTB was used as a loading control. (D–F) Quantification of ELP1 (D), ELP2 (E) and ELP3 (F) protein abundance from *Elp1*[cKO] and *Elp1*[WT] GCP lysates, normalized to ACTB. Unpaired *t*-tests. Mean ± SD. $N = \geq 3$ samples/genotype. (G) Sketch showing the Elongator core complex and its destabilization upon ELP1 loss. Adapted from Garcia-Lopez et al. (2021). (H) Percentage of proliferative GCPs (EdU+) after 72 h *in vitro* with Smoothened agonist (SAG). Unpaired *t*-test. Mean ± SD. $N = \geq 5$ samples/genotype. (I) Relative mRNA expression (quantitative PCR) of *Ccnd1*, *Ccnd2*, *Gli1*, *Gli2*, *Mycn*, *Ptch1* (SHH pathway genes), *Atoh1* (GCP marker) and *Elp1* of P7 GCPs after 72 h *in vitro* with SAG. Multiple Mann-Whitney *U* tests. Mean ± SD. $N \geq 4$ samples/genotype. (J) Total number of viable GCPs isolated from individual *Elp1*[WT] or *Elp1*[cKO] cerebella at P7. Unpaired *t*-test. $N = 13$ (WT) and 11 (cKO). (For interpretation of the references to colour in this figure legend, the reader is referred to the web version of this article.)

12 (Supplemental Tables S3-S5). In the SHIRPA screen at week 7, male *Elp1*[cKO] mice had similar scores to their *Elp1*[WT] littermates while female *Elp1*[cKO] mice had slightly worse overall scores than their *Elp1*[WT] littermates (Fig. 3B), but no significant differences were detected in any of the individual tests. Body weight and forelimb grip strength remained largely unchanged throughout the experimental period, although male mice showed a slight decrease at week 12 (Fig. 3C, D). Motor performance of *Elp1*[cKO] mice was significantly reduced in both sexes and at all time points (Fig. 3E), indicating a compromised motor performance compared with their control littermates.

To characterize the onset and progression of the ataxic gait, we performed a gait analysis using the CatWalk XT system (Fig. 3F; Heinzel et al. (2020); Pitzer et al. (2021)). Several gait parameters were disrupted in *Elp1*[cKO] mice compared with *Elp1*[WT] mice littermates, in particular in the hind paws (Fig. 3F-K). We detected a reduction in the area and the maximum intensity of the paw print, indicating that *Elp1*[cKO] animals placed less weight on a reduced area of their hind paws (Fig. 3G, H). These parameters were decreased in both sexes at all time points. Stride length and base-of-support are important distance parameters for assessing animal gait (Hamers et al., 2006) and are often compromised in patients with cerebellar ataxia (Palliyath et al., 1998; Stolze et al., 2002). *Elp1*[cKO] mice had a reduced stride length, indicating that the

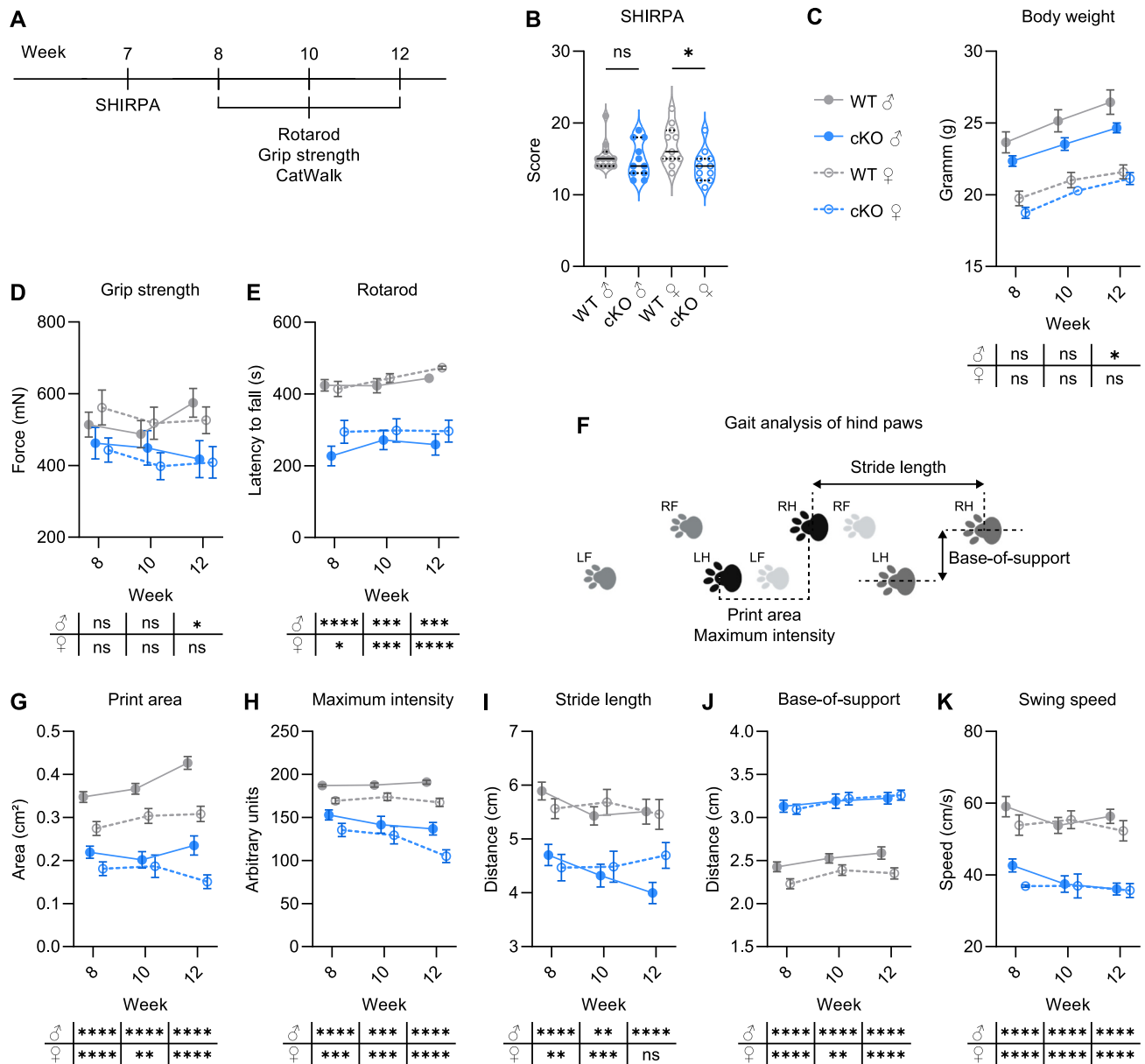Fig. 3. Adult *Elp1*cKO mice have impaired motor coordination and gait ataxia. (A) Schematic overview of the motor behavior tests. (B) SHIRPA score of male (filled circles) and female (empty circles) *Elp1*WT (gray) and *Elp1*cKO (blue) animals at week 7. (C) Average body weight of animals across sexes and time points. (D) Average grip strength across sexes and time points. (E) Average latency to fall in the rotarod test across sexes and time points. (F) Illustration of selected hind paw gait parameters. LF, left front paw. RF, right front paw. LH, left hind paw. RH, right hind paw. Adapted from Pitzer et al. (2021). (G-K) Quantification of hind paw gait parameters across sex and time points: print area (G), maximum intensity (H), stride length (I), base-of-support (J) and swing speed (K). (B-E; G-K) Mann-Whitney *U* tests. Mean ± SEM. *N* = 11 mice per time point, genotype and sex. (For interpretation of the references to colour in this figure legend, the reader is referred to the web version of this article.)

distance between consecutive placements of the same paw was reduced (Fig. 3I). *Elp1*cKO mice also had an increased base-of-support, such that animals increased the distance between both hind paws to better stabilize themselves (Fig. 3J), and a reduced swing speed in the hind paws (Fig. 3K), indicating a compromised motor coordination. In the forepaws, *Elp1*cKO animals exhibited an increased step cycle duration (paw stance and swing phase), increased swing phase and decreased swing speed (Supplemental Fig. S4A-C). Most of the significant phenotypes were already present at week 8. Furthermore, we did not observe any worsening of the parameters over time, suggesting that the cellular changes affecting the gait may occur at an earlier time point.

3.4. Cerebella of adult Elp1cKO ataxia mice are smaller, have fewer granule cells and show Purkinje cell abnormalities

Next, we investigated the underlying cellular changes driving the onset of the ataxia phenotype in *Elp1*cKO mice. Following the last behavioral measurements at 12 weeks of age, the animals were sacrificed and the gross morphology of the brains was analyzed (Fig. 4A). We found that *Elp1*cKO brains weighed less than brains of *Elp1*WT littermates (Fig. 4B). To investigate the possible origin of this phenotype, we quantified the surface areas of brain regions as an approximation of brain region size (Fig. 4A). While the surface area of the whole brain and the cortex remained unchanged, the surface area of the cerebellum was significantly reduced in *Elp1*cKO mice of both sexes (Fig. 4C-E). To determine the underlying cause of the reduced cerebellar size in
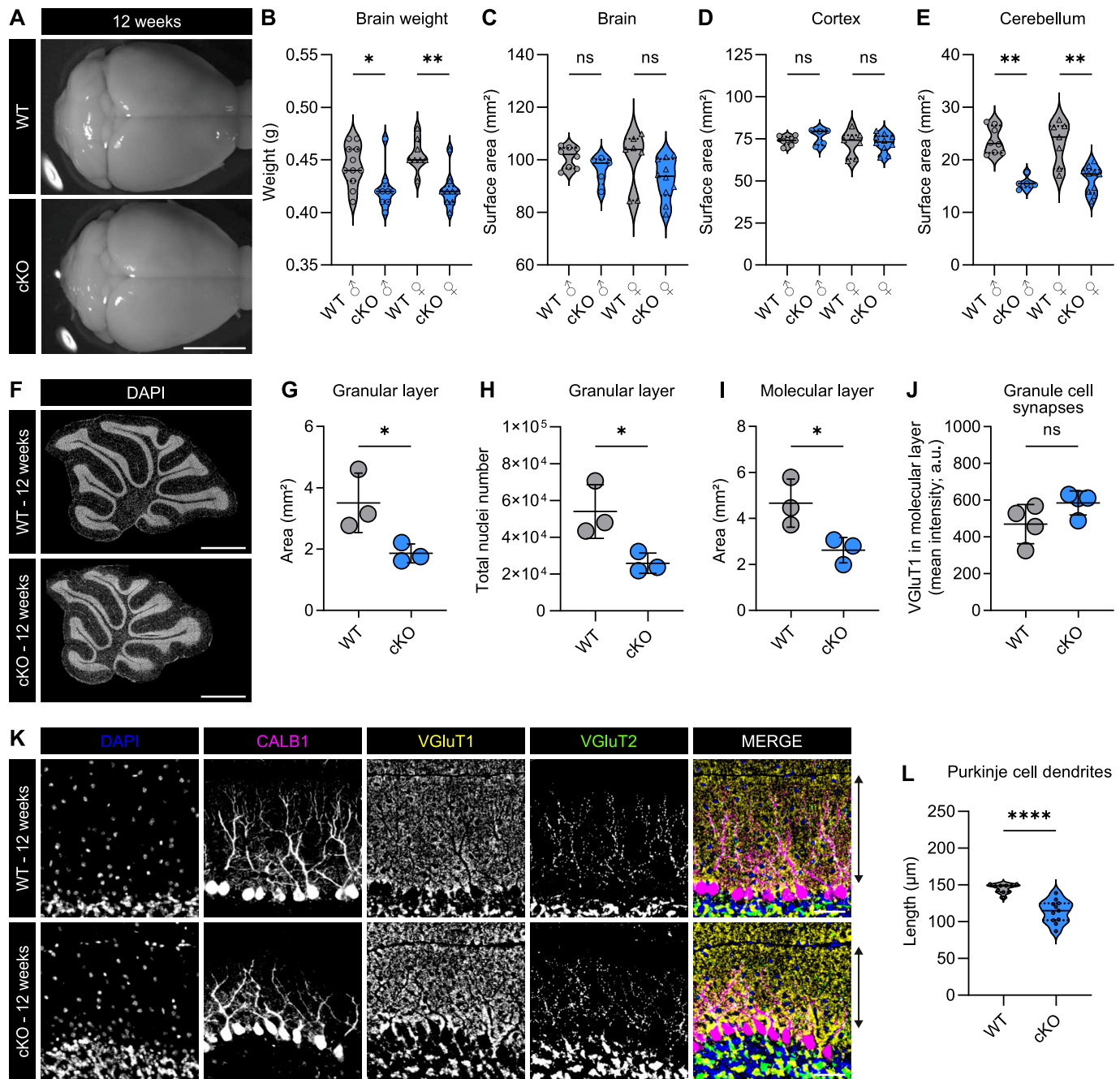
Fig. 4. Ataxic, 12-week-old *Elp1*^cKO mice have smaller cerebella, fewer GCs and a reduced area of the granular and molecular layers. (A) Representative brightfield images of brains of 12-week-old *Elp1*^WT and *Elp1*^cKO mice. Scale bar, 5 mm. (B) Total brain weight of 12-week-old *Elp1*^WT (gray) and *Elp1*^cKO (blue) mice. Mann-Whitney *U* test. $N \geq 8$ brains per genotype and sex. (C-E) Quantification of surface areas from brightfield images: whole brain (C), cortex (D) and cerebellum (E). Mann-Whitney *U* tests. $N = \geq 5$ brains per genotype and sex. (F–I) Representative nuclei (DAPI) staining of sagittal cerebellum section (F; scale bar, 1 mm) and quantification of granular layer area (G), total nuclei number in granular layer (H) and molecular layer area (I) in the whole cerebellum overview image. Mean ± SD. Unpaired *t*-test. $N = 3$ (J) Quantification of VGluT1 mean fluorescence intensity in the molecular layer of the whole cerebellum. Mean ± SD. Unpaired *t*-test. $N = 4$ (K) Representative immunofluorescence staining of DAPI (blue), CALB1 (magenta), VGluT1 (yellow) and VGluT2 (green) expression in lobule III of 12-week-old Elp1^WT and Elp1^cKO cerebella. The arrow indicates the width of the molecular layer. Scale bar, 50 μm. (L) Quantification of the maximum length of Purkinje cell dendrites. $N = 3$ mice/genotype, $n = \geq 3$ sections/mouse. (For interpretation of the references to colour in this figure legend, the reader is referred to the web version of this article.)

Elp1^cKO mice, we measured the area and total number of nuclei in the granular layer, molecular layer, and PC layer. We found that the area of the granular layer was reduced by about 47% in *Elp1*^cKO animals, and the total number of nuclei in the granular layer in one section was decreased by about 52% (Fig. 4F-H). The mean number of nuclei per mm² remained unchanged (Supplemental Fig. S5A). We observed a 25% decrease in the granular layer width in lobule III (Supplemental

Fig. S5B), suggesting that a decrease in width likely results in a decreased granular layer area. The large decrease in granular layer area and nuclei suggests a reduced total number of GCs in the *Elp1*^cKO cerebellum. Next, we measured the molecular layer, where parallel fibers from the GCs innervate the dendritic trees of PCs. Similar to the granular layer, *Elp1*cKO cerebella exhibit a reduced total area and width of the molecular layer (Fig. 4I; Supplemental Fig. S5C). We did not observe any

differences in the width of the PC layer (Supplemental Fig. S5D).

Because GCs form excitatory VGluT1+ synapses with PCs *via* their parallel fibers in the molecular layer (Leto et al., 2016), we hypothesized that the reduced pool of GCs would result in a reduced amount of VGluT1+ synapses. However, we did not observe any significant difference in the VGluT1+ fluorescence intensity at week 12 in the molecular layer (Fig. 4J, K; Supplemental Fig. S5E–F).

We also observed no differences in the density of climbing fiber synapses (VGluT2+) in the molecular layer and mossy fiber synapses

(VGluT1+ and/or VGluT2+) in the granular layer (Fig. 4K; Supplemental Fig. S5F–I). Pathological changes during development and/or loss of PCs have been shown to cause cerebellar ataxias (Leto et al., 2016). To determine whether the ataxia phenotype might be evoked by PC loss, we quantified the number of PCs in different lobules. We did not observe any significant differences in the overall morphology or density of PCs between *Elp1*cKO and *Elp1*WT animals (Fig. 4K, Supplemental Fig. S5F, J). Consistent with the reduced width of the molecular layer, the length of *Elp1*cKO PC dendrites was also reduced (Fig. 4K, L).
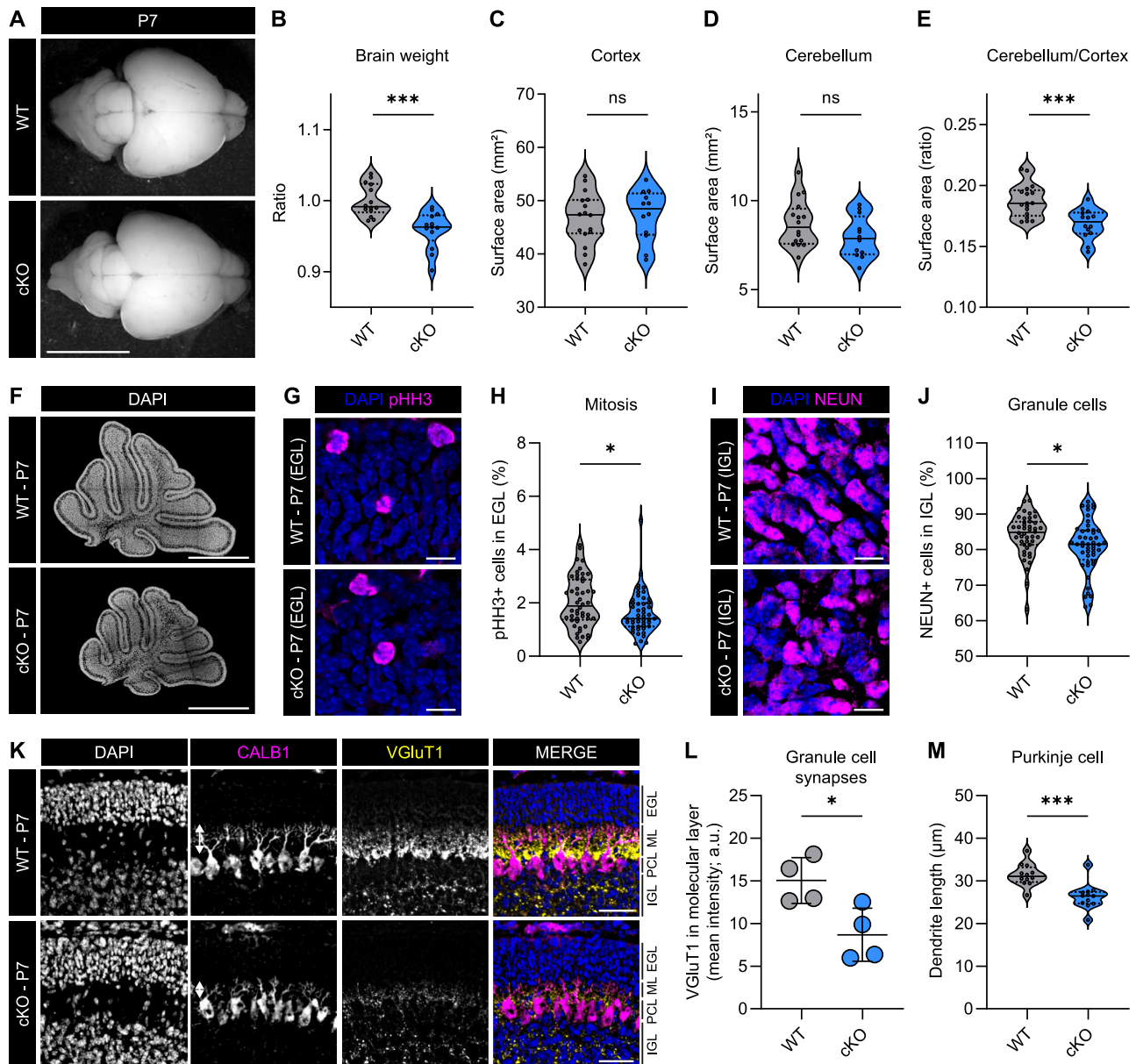

Fig. 5. P7 *Elp1*cKO mice show delayed GC maturation, resulting in reduced cerebellar size. (A) Representative brightfield images of *Elp1*WT and *Elp1*cKO brains at P7. Scale bar, 5 mm. (B) Quantification of *Elp1*cKO and *Elp1*WT brain weights at P7. Mann-Whitney *U* test. $N = 14$ (WT) and 13 (cKO). (C-E) Quantification of surface areas from brightfield images: cortex (C), cerebellum (D) and cerebellum/cortex ratio (E). Unpaired *t*-tests. $N = 16$ (WT) and 12 (cKO). (F) Representative nuclei staining (DAPI) of sagittal section of whole cerebellum. Scale bar, 1 mm. (G,H) Representative immunofluorescence staining (G) and quantification of DAPI (blue) and mitosis marker pHH3 (magenta; H) in the EGL of lobules III, VI, IX and X at P7. Scale bar, 10 μm. $N = 3$ mice/genotype, $n = 4$ sections/lobule. (I-J) Representative immunofluorescence staining against DAPI (blue) and granule cell marker NEUN (magenta) in the IGL of lobule III (I) and quantification (J) of NEUN+ GCs in the IGL of lobules III, VI, IX and X at P7. Scale bar, 10 μm. $N = 3$ mice/genotype, $n = 4$ sections/lobule. (K) Representative immunofluorescence staining of DAPI (blue), Purkinje cell marker CALB1 (magenta) and granule cell synapse marker VGluT1 (yellow) at P7. Scale bar, 50 μm. Arrows in the CALB1 panel indicate the length of the Purkinje cell dendrites. IGL, internal granular layer. PCL, Purkinje cell layer. ML, molecular layer. EGL, external granular layer. (L) Quantification of VGluT1 mean fluorescence intensity in the molecular layer of the whole cerebellum at P7. Mean ± SD. Unpaired *t*-test. $N = 4$ mice/genotype. (M) Quantification of Purkinje cell dendrite length in lobule VI. Mann-Whitney U test. $N = 3$ mice/genotype, $n = 4$ sections/mouse. (For interpretation of the references to colour in this figure legend, the reader is referred to the web version of this article.)

Taken together, 12-week-old *Elp1*[cKO] animals had smaller cerebella, most likely caused by a reduction in the granular and molecular layers *via* a decrease in the total number of GCs in the *Elp1*[cKO] cerebella. Notably, we did not observe any differences in the number of PCs, but the dendritic complexity of PCs might be compromised due to shorter dendrites and reduced GC synaptic inputs, suggesting abnormal PC development as a result of defects in GC development.

3.5. Early postnatal Elp1[cKO] mice have smaller cerebella

Because the total number of GCs was the only major defect we identified at 12 weeks, we next examined animals before the onset of ataxia to determine when the number of GCs was reduced. Similar to 12-week-old mice, P28 *Elp1*[cKO] mice had smaller cerebella with a reduced area and fewer nuclei in the granular layer (Supplemental Fig. S6A–D), whereas no changes were detected in the molecular layer (Supplemental Fig. S6A, E).

Next, we examined the effect of *Elp1* loss on the GC lineage at P7, when GCP proliferation in the EGL peaks (Consalez et al., 2021). First, we assessed the motor control and coordination of P7 pups by testing the righting reflex (Feather-Schussler and Ferguson, 2016); at P5, mouse pups are able to flip from a supine position onto their paws (Heyser, 2003). *Elp1*[cKO] pups had proper righting reflexes (Supplemental Fig. S7A), suggesting no motor defects at this age. We next examined the overall brain size and cellular composition of *Elp1*[cKO] animals. We observed a reduced total weight of *Elp1*[cKO] brains compared with their control littermates (Fig. 5A-B). While the total surface areas of brain, cortex and cerebellum did not change (Fig. 5C, D; Supplemental Fig. S7B), the ratio of cerebellum/cortex area was significantly reduced in *Elp1*[cKO] mice (Fig. 5E), suggesting a slightly smaller cerebellum already at P7.

At the cellular level, immunofluorescence staining revealed no significant differences in the area or number of nuclei in the EGL, IGL or ML (Supplemental Fig. S7C-G). In the EGL, the number of GCPs (PAX6+) was unchanged (Supplemental Fig. S7H, I) but slightly fewer mitotic GCPs (pHH3+) were present in *Elp1*[cKO] cerebella (Fig. 5G, H). However, no significant differences in the number of cycling (MKI67+), S-phase (EdU+) or cell cycle exiting GCPs (EdU+MKI67-/EdU+) were detected (Supplemental Fig. S7J-M), consistent with the *in vitro* assay results above (Fig. 2H).

Upon differentiation, GCPs migrate inward into the IGL and become mature NEUN+ GCs. Immunofluorescence imaging revealed a significant decrease in NEUN+ GCs in the *Elp1*[cKO] IGL (Fig. 5I, J). In addition, *Elp1*[cKO] cerebella expressed significantly lower levels of VGluT1 in the molecular layer (Fig. 5K, L; Supplemental Fig. S8A), further confirming fewer mature GCs in *Elp1*[cKO] mice at P7. Furthermore, a lower density of VGluT1+ mossy fiber synapses was present in the IGL, whereas VGluT2+ synapses (mossy fiber) in the IGL and VGluT2+ synapses in both the IGL (mossy fiber) and molecular layer (climbing fiber) were unaffected (Fig. 5K; Supplemental Fig. S8A–D). Total PC numbers were unchanged; instead, dendrite length was reduced in *Elp1*[cKO] animals (Fig. 5K, M). Taken together, P7 *Elp1*[cKO] cerebella display a delay in GC maturation, as the total number of GCPs in the EGL are unchanged, while the number of mature GCs are reduced. This delay is likely to be an underlying cause of the reduction in cerebellar size.

3.6. Elp1[cKO] increases cell cycle inhibition, apoptosis and reduces differentiation

ELP1 is the scaffolding subunit of the Elongator complex, which catalyzes the addition of 5-carboxymethyl derivatives to tRNAs and modulates protein expression during translation. Previous work has shown that *ELP1* loss can lead to various outcomes such as protein misfolding and aggregation, the activation of the unfolded protein response, codon-dependent translational reprogramming and/or the disruption of protein homeostasis (Goffena et al., 2018; Laguesse et al.,

2015; Nedialkova and Leidel, 2015; Waszak et al., 2020). Therefore, we measured Elongator-dependent tRNA modifications (mcm[5], ncm[5] and mcm[5]s[2]) from *Elp1*[cKO] and *Elp1*[WT] bulk GCPs isolated from P7 cerebellum. However, we did not detect changes in these modifications (Supplemental Fig. S9A–C), likely because of their low abundance in bulk tRNA and/or the incomplete *Elp1* knockout in GCPs in the nodular lobules IX or X (Fig. 2B).

To identify the molecular causes underlying the delay in GC maturation and reduced number of mature GCs, we performed bulk RNA sequencing of P7 *Elp1*[WT] and *Elp1*[cKO] GCPs (Fig. 6A; Supplemental Table S6). As expected, *Elp1* transcript levels were significantly reduced. We found that the neurite outgrowth factor gene *Gprin3* and *VGluT1* expression were strongly reduced in *Elp1*[cKO] GCPs, the latter providing a molecular basis for reduced protein expression in mature GCs at P7 (Fig. 5K, L). Furthermore, the cellular stress genes *Asns* and *Sesn2*, the pro-apoptotic factor genes *Aen* and *Pmaip1* (also called *Noxa*), and the unfolded protein response pathway gene *Chac1* showed a significant upregulation in *Elp1*[cKO] GCPs (Fig. 6A). In addition, the expression of the cell cycle inhibitor gene *Cdkn1a* (or *P21*) was highly upregulated in *Elp1*[cKO] GCPs. Gene Set Enrichment Analysis (GSEA; Subramanian et al. (2005)) of the transcriptomic data revealed significant upregulation of the P53-mediated apoptosis pathway and downregulation of neuronal development and synaptic transmission pathways (Fig. 6B; Supplemental Fig. S9D), indicating impaired neuronal maturation in *Elp1*[cKO] GCPs. Overall, *Elp1*[cKO] GCP transcriptomes show increased expression of cell cycle inhibitors, stress sensors and pro-apoptotic factors, suggesting an increased intrinsic cell stress in *Elp1*[cKO] GCPs.

To examine changes at the protein level, we performed tandem mass tag-mass spectrometry proteomics on samples isolated from the same cerebella used for transcriptome profiling. Proteomic analysis validated the significant reduction of ELP1, ELP2, and ELP3 protein levels, confirming the destabilization of the Elongator complex (Fig. 6C; Supplemental Fig. S9E; Supplemental Table S6). Upregulation of the stress sensor ASNS and the apoptosis promoting nuclease AEN suggested increased cell death in *Elp1*[cKO] GCPs. Furthermore, proteomic GSEA revealed the significant downregulation of biological processes related to tRNA modification, DNA replication and DNA damage repair (Fig. 6D), common pathways frequently associated with Elongator loss.

To verify that *Elp1*[cKO] GCPs undergo cell stress leading to cell death, we performed immunofluorescence staining against cleaved-CASP3, the functional unit of the cell death effector gene *Caspase3*. Indeed, we confirmed a marked increase in dying GCPs in the EGL of *Elp1*[cKO] mice compared with *Elp1*[WT] sibling controls (Fig. 6E, F). The number of cleaved-CASP3+ GCs in the IGL remained unchanged (Fig. 6E; Supplemental Fig. S9F), highlighting that *Elp1* loss resulted in cell death predominantly in GCPs.

The increased expression of cleaved-CASP3 was further confirmed by immunoblotting of purified GCPs (21-fold increase; Fig. 6G; Supplemental Fig. S9G). We also confirmed increased P21 protein levels, with a 5-fold increase in *Elp1*[cKO] GCPs (Fig. 6G; Supplemental Fig. S9H). Taken together, the combined increase in P21 and cleaved-CASP3 in *Elp1*[cKO] GCPs suggests activation of cell cycle inhibition, leading to cell death and ultimately to a reduced number of GCPs and subsequent mature GC pool. Reduced GCP differentiation was also confirmed by lower levels of the mature GC markers NEUN, NEUROD1 and VGluT1 (Fig. 6G; Supplemental Fig. S9I-L).

Taken together, loss of *Elp1* in GCPs increased cell cycle inhibition and cell death pathways and decreased terminal differentiation to GCs. Both processes likely reduce the final pool of functional GCs and, consequently, functional synapses with PCs, eventually leading to the gradual onset of ataxia (Fig. 6H).
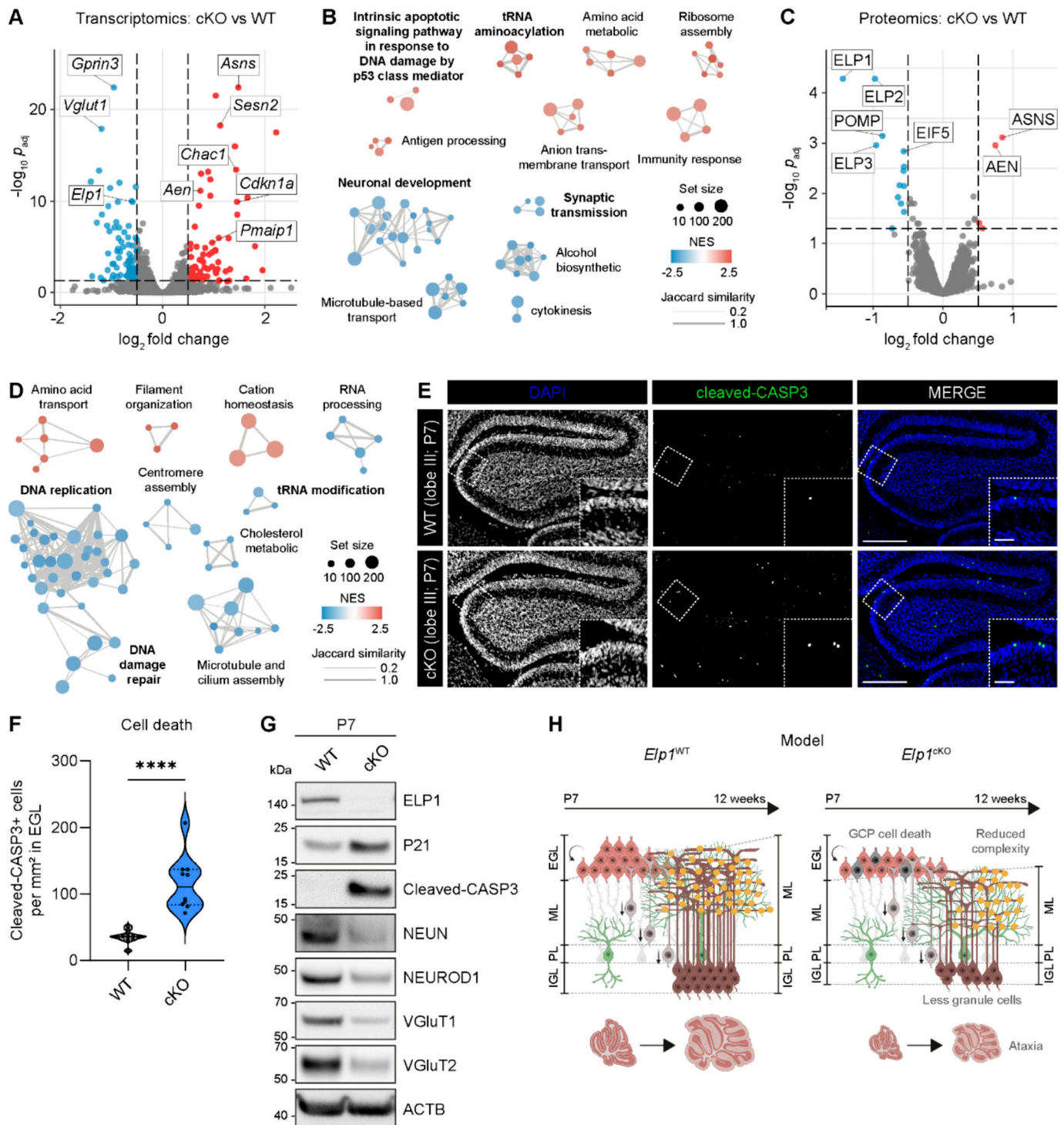
Fig. 6. *Elp1*^cKO increases cell cycle inhibition and cell death in GCPs and decreases GC differentiation. (A) Volcano plot of bulk RNA-seq of P7 *Elp1*^cKO *vs Elp1*^WT GCPs showing up- (red) and downregulated (blue) genes. $N = 4$ samples/genotype. Cutoffs: log$_2$ fold change = 0.5 and -log$_{10}$ p_{adj} = 0.05. (B) Network visualization of GSEA of transcriptomes showing up- (red) and downregulated (blue) biological processes. Dot size represents gene set size. $p_{adj} < 0.05$. NES, normalized enrichment score. (C) Volcano plot of proteomics, highlighting up- (red) and downregulated (blue) proteins in P7 *Elp1*^cKO *vs Elp1*^WT GCPs. $N = 4$ samples/genotype. Cutoffs: log$_2$ fold change = 0.5 and -log$_{10}$ p_{adj} = 0.05. Paired samples were used for transcriptome and proteome profiling. (D) Proteome network analysis showing up- (red) and downregulated (blue) biological processes. $p_{adj} < 0.05$. (E) Representative immunofluorescence staining of DAPI (blue) and cell death marker cleaved-CASP3 (green) in lobule III. Single z-slice. Scale bar, 250 μm. Inset, scale bar, 50 μm. (F) Quantification of cleaved-CASP3 positive cells in the external granular layer (EGL) of the whole cerebellum. Mann-Whitney *U* test. $N = 3$ mice/genotype. $n = 2$–4 sections. (G) Immunoblot validation of ELP1, P21, cleaved-CASP3, NEUN, NEUROD1, VGluT1, VGluT2 and ACTB protein abundance in lysates from *Elp1*^WT and *Elp1*^cKO GCPs at P7. (H) Schematic model of ataxia onset by *Elp1*^cKO in GCPs, presumably by GCP cell death in early stages, resulting in a reduced GC pool, reduced GC-PC synaptic complexity and smaller cerebellum size. (For interpretation of the references to colour in this figure legend, the reader is referred to the web version of this article.)

4. Discussion

4.1. Role of granule cells in motor behavior and ataxia

Using an *Atoh1-Cre* mouse line, we removed *Elp1* in the majority of the cerebellar GCPs. Adult mice developed ataxia, which we propose is the result of increased cell death of GCPs in early postnatal stages, leading to a decrease in mature GCs as the animals age. While pathological changes or loss of PCs are well-established drivers of cerebellar ataxia (Becker et al., 2009; Hansen et al., 2013; Hourez et al., 2011; Todorov et al., 2012; Tsai et al., 2012), manipulation of GCs has also been shown to impair motor coordination and induce signs of cerebellar ataxia (Galliano et al., 2013; Kim et al., 2009; Lee et al., 2023; Miyazaki et al., 2021; Wada et al., 2007; Yamamoto et al., 2003). In our model, the defects in both GCs and PCs were subtle in adult *Elp1*^{cKO} animals, although the ataxia phenotype was strong. In recent studies, GCs were either selectively ablated or functionally silenced, resulting in severe motor deficits affecting balance, coordination and gait (Lee et al., 2023; Miyazaki et al., 2021). While selective GC ablation reduced cerebellar size and the width of both the GL and ML, PC death was not evident and overall PC firing rates were unaffected (Lee et al., 2023; Miyazaki et al., 2021). Correspondingly, the number of PCs in *Elp1*^{cKO} cerebella were unchanged, and only the length of the dendrites was reduced, which might be caused by a reduction in the width of the molecular layer. Together with our results, recent studies suggest that reduced GC signaling by depletion of synaptic transmission or by reduction of the total GC pool leads to motor deficits, while leaving PC function largely intact (Lee et al., 2023; Miyazaki et al., 2021).

4.2. ELP1 function in granule cells: a potential link to Familial Dysautonomia?

FD patients typically present with progressive ataxias (Portnoy et al., 2018) although the underlying cause of the ataxia is unclear. In FD patients, loss of muscle spindle afferents in the peripheral nervous system plays a role in the ataxic gait (Macefield et al., 2011). While white matter loss has been observed in the cerebellar peduncles, the cerebellar vermis of FD patients does not have an obvious reduction in size (Axelrod et al., 2010). In older patients, however, generalized atrophy may occur in the cerebellum (Axelrod and Gold-von Simson, 2007; Cohen and Solomon, 1955). Recently, Kojic et al. (2023) reported two *ELP1*-deficient patients with white matter lesions in the cerebral hemispheres, suggesting a prominent role of *ELP1* in neurodevelopmental diseases and overall brain health. Our studies demonstrate a central role of *Elp1* in maintaining GC (progenitor) health and a functional cerebellum. Given that *ELP1* mis-splicing occurs predominantly in the cerebellum of FD patients (Hims et al., 2007) and the observation that cerebellar atrophy occurs with age (Axelrod and Gold-von Simson, 2007), *ELP1* loss in the cerebellum of FD patients may indeed play a role, albeit likely minor, in maintaining balance and coordination. Future studies in FD patients and patient-derived cells would be required to confirm this putative role.

4.3. ELP1 and Elongator are crucial for cerebellar neurodevelopment and maintenance

In mouse models, homozygous loss of *Elp1* is embryonic lethal by E12.5, with severe developmental delay, heart and brain defects, and incomplete neurulation (Chen et al., 2009; Dietrich et al., 2011). CNS-specific knockout of *Elp1* using a *Tuba1a-Cre* mouse line resulted in reduced ELP1 expression in the striatum and cortex (Chaverra et al., 2017). While the effect on the cerebellum was not explicitly examined in this mouse model, the animals had a slow and unsteady gait. *Elp1* was also critical for cell survival of spinal motor neurons and cortical neurons (Chaverra et al., 2017). Similarly, knockout of *Elp1* in neural crest-derived neurons resulted in increased neuronal cell death of selective populations and in reduced nerve growth during development (George et al., 2013; Jackson et al., 2014; Leonard et al., 2022). Notably, both transcript and protein levels of the asparagine synthetase *Asns* were upregulated in *Elp1*^{cKO} GCPs, consistent with its increased expression in the degenerating dorsal root ganglia of another FD-specific mouse model (Harripaul et al., 2024). Increased expression of tRNA synthetases has been associated with peripheral neurodegeneration (Burgess and Storkebaum, 2023); however, our study identifies a similar correlation in CNS neurons, but the mechanistic link between *Elp1* and *Asns* remains elusive. Taken together, these published studies and our current work confirm the essential role of *Elp1* in maintaining neuronal survival as a key function in maintaining brain health. Whether this neuronal cell death results from the direct or indirect effect of impaired tRNA modifications remains unknown (Ueki et al., 2018); however, it is clear that only certain classes of neurons are sensitive to *Elp1* loss. Future work is needed to determine the underlying mechanisms of this sensitivity.

Other members of the Elongator complex have also been implicated in neurodevelopmental disorders, including intellectual disability and autism spectrum disorders (Addis et al., 2015; Kojic et al., 2021), suggesting a central role for this complex in CNS development. Patient-derived germline mutations of *Elp2* in mice cause gait defects, although specific defects in the cerebellum have not been identified (Kojic et al., 2021). However, mice with a germline mutation in *ELP6* develop ataxia, likely as a result of PC degeneration (Kojic et al., 2018). Altogether, the Elongator complex plays a critical role in developing and maintaining health of cerebellar neurons.

5. Conclusion

In this paper, we investigated the role of the Elongator complex protein ELP1 in the development of cerebellar granule cells, which constitute the vast majority of neurons in the adult brain. We could show that ELP1 is highly expressed in proliferating GCPs and that its loss destabilizes the Elongator complex and induces GCP cell death, reducing the pool of mature granule cells and the size of the cerebellum. Furthermore, GCP-specific loss of *Elp1* triggered the onset of ataxia in mice, and gait analysis resembled the ataxic phenotype of Familial Dysautonomia patients. Our study highlights the importance of the Elongator complex for the generation and maintenance of granule cells in the cerebellum.

Funding

CRediT authorship contribution statement

Frederik Arnskötter: Writing – review & editing, Writing – original draft, Visualization, Validation, Investigation, Formal analysis. **Patricia Benites Goncalves da Silva:** Writing – review & editing, Investigation, Formal analysis. **Mackenna E. Schouw:** Writing – review & editing, Investigation. **Chiara Lukasch:** Investigation. **Luca Bianchini:** Writing – review & editing, Investigation. **Laura Sieber:** Investigation. **Jesus Garcia-Lopez:** Investigation. **Shiekh Tanveer Ahmad:** Writing – review & editing, Investigation. **Yiran Li:** Formal analysis. **Hong Lin:** Writing – review & editing, Investigation. **Piyush Joshi:** Writing – review & editing, Formal analysis. **Lisa Spänig:** Investigation. **Magdalena Radoš:** Writing – review & editing, Investigation. **Mykola Roiuk:** Writing – review & editing, Investigation. **Mari Sepp:** Writing – review & editing, Formal analysis. **Marc Zuckermann:** Writing – review & editing, Resources. **Paul A. Northcott:** Writing – review & editing, Resources, Formal analysis. **Annarita Patrizi:** Writing – review & editing, Visualization, Investigation. **Lena M. Kutscher:** Writing – review & editing, Writing – original draft, Supervision, Funding acquisition, Formal analysis, Conceptualization.

Declaration of competing interest

The authors declare that they have no competing interests.

Data availability

All processed data is included in Supplemental Tables within the manuscript. Raw sequencing data will be made available upon request.

Appendix A. Supplementary data

Supplementary data to this article can be found online at https://doi.org/10.1016/j.nbd.2024.106600.

References

Abbassi, N.-E.-H., et al., 2024. Cryo-EM structures of the human Elongator complex at work. Nat. Commun. 15, 4094.

Addis, L., et al., 2015. Microdeletions of ELP4 are associated with language impairment, autism spectrum disorder, and mental retardation. Hum. Mutat. 36, 842–850.

Anderson, S.L., et al., 2001. Familial dysautonomia is caused by mutations of the IKAP gene. Am. J. Hum. Genet. 68, 753–758.

Axelrod, F.B., Gold-von Simson, G., 2007. Hereditary sensory and autonomic neuropathies: types II, III, and IV. Orphanet J. Rare Dis. 2, 1–12.

Axelrod, F.B., et al., 2002. Survival in familial dysautonomia: impact of early intervention. J. Pediatr. 141, 518–523.

Axelrod, F.B., et al., 2010. Neuroimaging supports central pathology in familial dysautonomia. J. Neurol. 257, 198–206.

Bai, B., et al., 2017. Quantitative phosphoproteomic analysis of brain tissues. Neuroproteomics: Methods Protocols 199–211.

Becker, E.B., et al., 2009. A point mutation in TRPC3 causes abnormal Purkinje cell development and cerebellar ataxia in moonwalker mice. Proc. Natl. Acad. Sci. 106, 6706–6711.

Burgess, R.W., Storkebaum, E., 2023. tRNA dysregulation in neurodevelopmental and neurodegenerative diseases. Annu. Rev. Cell Dev. Biol. 39, 223–252.

Cardoso-Moreira, M., et al., 2019. Gene expression across mammalian organ development. Nature 571, 505–509.

Chaverra, M., et al., 2017. The familial dysautonomia disease gene IKBKAP is required in the developing and adult mouse central nervous system. Dis. Model. Mech. 10, 605–618.

Chen, Y.-T., et al., 2009. Loss of mouse Ikbkap, a subunit of elongator, leads to transcriptional deficits and embryonic lethality that can be rescued by human IKBKAP. Mol. Cell. Biol. 29, 736–744.

Cohen, P., Solomon, N.H., 1955. Familial dysautonomia: case report with autopsy. J. Pediatr. 46, 663–670.

Consalez, G.G., et al., 2021. Origins, development, and compartmentation of the granule cells of the cerebellum. Front. Neural Circ. 88.

Cuajungco, M.P., et al., 2003. Tissue-specific reduction in splicing efficiency of IKBKAP due to the major mutation associated with familial dysautonomia. Am. J. Hum. Genet. 72, 749–758.

Dietrich, P., et al., 2011. Deletion of exon 20 of the familial Dysautonomia gene Ikbkap in mice causes developmental delay, cardiovascular defects, and early embryonic lethality. PLoS One 6, e27015.

Dietrich, P., et al., 2012. IKAP expression levels modulate disease severity in a mouse model of familial dysautonomia. Hum. Mol. Genet. 21, 5078–5090.

Dobin, A., et al., 2013. STAR: ultrafast universal RNA-seq aligner. Bioinformatics 29, 15–21.

Eltokhi, A., et al., 2021. Comprehensive characterization of motor and coordination functions in three adolescent wild-type mouse strains. Sci. Rep. 11, 6497.

Feather-Schussler, D.N., Ferguson, T.S., 2016. A battery of motor tests in a neonatal mouse model of cerebral palsy. JoVE (J. Visual. Exper.) 117, e53569.

Galliano, E., et al., 2013. Silencing the majority of cerebellar granule cells uncovers their essential role in motor learning and consolidation. Cell Rep. 3, 1239–1251.

Garcia-Lopez, J., et al., 2021. Deconstructing sonic hedgehog medulloblastoma: molecular subtypes, drivers, and beyond. Trends Genet. 37, 235–250.

George, L., et al., 2013. Familial dysautonomia model reveals Ikbkap deletion causes apoptosis of Pax3+ progenitors and peripheral neurons. Proc. Natl. Acad. Sci. 110, 18698–18703.

Goffena, J., et al., 2018. Elongator and codon bias regulate protein levels in mammalian peripheral neurons. Nat. Commun. 9, 889.

González-Duarte, A., et al., 2023. Familial dysautonomia. Clin. Auton. Res. 1–12.

Gutiérrez, J.V., et al., 2015. Brainstem reflexes in patients with familial dysautonomia. Clin. Neurophysiol. 126, 626–633.

Haag, D., et al., 2021. H3. 3-K27M drives neural stem cell-specific gliomagenesis in a human iPSC-derived model. Cancer Cell 39, 407–422 (e13).

Hamers, F.P., et al., 2006. CatWalk-assisted gait analysis in the assessment of spinal cord injury. J. Neurotrauma 23, 537–548.

Hansen, S.T., et al., 2013. Changes in Purkinje cell firing and gene expression precede behavioral pathology in a mouse model of SCA2. Hum. Mol. Genet. 22, 271–283.

Harripaul, R., et al., 2024. Transcriptome analysis in a humanized mouse model of familial dysautonomia reveals tissue-specific gene expression disruption in the peripheral nervous system. Sci. Rep. 14, 570.

Hatten, M.E., 1985. Neuronal regulation of astroglial morphology and proliferation in vitro. J. Cell Biol. 100, 384–396.

Heinzel, J., et al., 2020. Use of the CatWalk gait analysis system to assess functional recovery in rodent models of peripheral nerve injury–a systematic review. J. Neurosci. Methods 345, 108889.

Heyser, C.J., 2003. Assessment of developmental milestones in rodents. Curr. Protoc. Neurosci. 25, 8.18. 1-8.18. 15.

Hims, M.M., et al., 2007. A humanized IKBKAP transgenic mouse models a tissue-specific human splicing defect. Genomics 90, 389–396.

Hourez, R., et al., 2011. Aminopyridines correct early dysfunction and delay neurodegeneration in a mouse model of spinocerebellar ataxia type 1. J. Neurosci. 31, 11795–11807.

Jackson, M.Z., et al., 2014. A neuron autonomous role for the familial dysautonomia gene ELP1 in sympathetic and sensory target tissue innervation. Development 141, 2452–2461.

Karlsborn, T., et al., 2014. Familial dysautonomia (FD) patients have reduced levels of the modified wobble nucleoside mcm5s2U in tRNA. Biochem. Biophys. Res. Commun. 454, 441–445.

Kawauchi, D., et al., 2012. A mouse model of the most aggressive subgroup of human medulloblastoma. Cancer Cell 21, 168–180.

Kim, J.C., et al., 2009. Linking genetically defined neurons to behavior through a broadly applicable silencing allele. Neuron 63, 305–315.

Kojic, M., et al., 2018. Elongator mutation in mice induces neurodegeneration and ataxia-like behavior. Nat. Commun. 9, 3195.

Kojic, M., et al., 2021. Elp2 mutations perturb the epitranscriptome and lead to a complex neurodevelopmental phenotype. Nat. Commun. 12, 2678.

Kojic, M., et al., 2023. A novel ELP1 mutation impairs the function of the Elongator complex and causes a severe neurodevelopmental phenotype. J. Hum. Genet. 68, 445–453.

Kozareva, V., et al., 2021. A transcriptomic atlas of mouse cerebellar cortex comprehensively defines cell types. Nature 598, 214–219.

Kutscher, L.M., et al., 2020. Functional loss of a noncanonical BCOR–PRC1. 1 complex accelerates SHH-driven medulloblastoma formation. Genes Dev. 34, 1161–1176.

Laguesse, S., et al., 2015. A dynamic unfolded protein response contributes to the control of cortical neurogenesis. Dev. Cell 35, 553–567.

Langlieb, J., et al., 2023. The molecular cytoarchitecture of the adult mouse brain. Nature 624, 333–342.

Lee, J.-H., et al., 2023. Cerebellar granule cell signaling is indispensable for normal motor performance. Cell Rep. 42.

Leonard, C.E., et al., 2022. Loss of Elp1 disrupts trigeminal ganglion neurodevelopment in a model of familial dysautonomia. Elife 11, e71455.

Leto, K., et al., 2016. Consensus paper: cerebellar development. Cerebellum 15, 789–828.

Liberzon, A., et al., 2011. Molecular signatures database (MSigDB) 3.0. Bioinformatics 27, 1739–1740.

Love, M.I., et al., 2014. Moderated estimation of fold change and dispersion for RNA-seq data with DESeq2. Genome Biol. 15, 1–21.

Macefield, V.G., et al., 2011. Can loss of muscle spindle afferents explain the ataxic gait in Riley–Day syndrome? Brain 134, 3198–3208.

Matei, V., et al., 2005. Smaller inner ear sensory epithelia in Neurog1 null mice are related to earlier hair cell cycle exit. Dev. Dyn. 234, 633–650.

Mendoza-Santiesteban, C.E., et al., 2012. Clinical neuro-ophthalmic findings in familial dysautonomia. J. Neuro-Ophthalmol.: Off. J. North Am. Neuro-Ophthalmol. Soc. 32, 23.

Miyazaki, T., et al., 2021. Excitatory and inhibitory receptors utilize distinct post-and trans-synaptic mechanisms in vivo. Elife 10, e59613.

Morini, E., et al., 2016. Sensory and autonomic deficits in a new humanized mouse model of familial dysautonomia. Hum. Mol. Genet. 25, 1116–1128.

Morini, E., et al., 2023. Development of an oral treatment that rescues gait ataxia and retinal degeneration in a phenotypic mouse model of familial dysautonomia. Am. J. Hum. Genet. 110, 531–547.

Nedialkova, D.D., Leidel, S.A., 2015. Optimization of codon translation rates via tRNA modifications maintains proteome integrity. Cell 161, 1606–1618.

Pagala, V.R., et al., 2015. Quantitative Protein Analysis by Mass Spectrometry. Protein-Protein Interactions: Methods and Applications, pp. 281–305.

Palliyath, S., et al., 1998. Gait in patients with cerebellar ataxia. Move. Disord.: Off. J. Move. Disord. Soc. 13, 958–964.

Pan, N., et al., 2009. Defects in the cerebella of conditional Neurod1 null mice correlate with effective Tg (Atoh1-cre) recombination and granule cell requirements for Neurod1 for differentiation. Cell Tissue Res. 337, 407–428.

Pitzer, C., et al., 2021. Gait performance of adolescent mice assessed by the CatWalk XT depends on age, strain and sex and correlates with speed and body weight. Sci. Rep. 11, 21372.

Portnoy, S., et al., 2018. Characteristics of ataxic gait in familial dysautonomia patients. PLoS One 13, e0196599.

Rodríguez, C.I., et al., 2000. High-efficiency deleter mice show that FLPe is an alternative to Cre-loxP. Nat. Genet. 25, 139–140.

Rogers, D.C., et al., 1997. Behavioral and functional analysis of mouse phenotype: SHIRPA, a proposed protocol for comprehensive phenotype assessment. Mamm. Genome 8, 711–713.

Rotthier, A., et al., 2012. Mechanisms of disease in hereditary sensory and autonomic neuropathies. Nat. Rev. Neurol. 8, 73–85.

Schindelin, J., et al., 2012. Fiji: an open-source platform for biological-image analysis. Nat. Methods 9, 676–682.

Schmahmann, J.D., 2019. The cerebellum and cognition. Neurosci. Lett. 688, 62–75.

Sepp, M., et al., 2024. Cellular development and evolution of the mammalian cerebellum. Nature 625, 788–796.

Slaugenhaupt, S.A., et al., 2001. Tissue-specific expression of a splicing mutation in the IKBKAP gene causes familial dysautonomia. Am. J. Hum. Genet. 68, 598–605.

Stolze, H., et al., 2002. Typical features of cerebellar ataxic gait. J. Neurol. Neurosurg. Psychiatry 73, 310–312.

Subramanian, A., et al., 2005. Gene set enrichment analysis: a knowledge-based approach for interpreting genome-wide expression profiles. Proc. Natl. Acad. Sci. 102, 15545–15550.

Todorov, B., et al., 2012. Purkinje cell-specific ablation of ca V 2.1 channels is sufficient to cause cerebellar ataxia in mice. Cerebellum 11, 246–258.

Tsai, P.T., et al., 2012. Autistic-like behaviour and cerebellar dysfunction in Purkinje cell Tsc1 mutant mice. Nature 488, 647–651.

Ueki, Y., et al., 2018. Retina-specific loss of Ikbkap/Elp1 causes mitochondrial dysfunction that leads to selective retinal ganglion cell degeneration in a mouse model of familial dysautonomia. Dis. Model. Mech. 11, dmm033746.

Wada, N., et al., 2007. Conditioned eyeblink learning is formed and stored without cerebellar granule cell transmission. Proc. Natl. Acad. Sci. 104, 16690–16695.

Wang, X., et al., 2014. JUMP: a tag-based database search tool for peptide identification with high sensitivity and accuracy. Mol. Cell. Proteomics 13, 3663–3673.

Waszak, S.M., et al., 2020. Germline elongator mutations in sonic hedgehog medulloblastoma. Nature 580, 396–401.

Wechsler-Reya, R.J., Scott, M.P., 1999. Control of neuronal precursor proliferation in the cerebellum by sonic hedgehog. Neuron 22, 103–114.

Wu, T., et al., 2021. clusterProfiler 4.0: a universal enrichment tool for interpreting omics data. Innovation 2.

Xu, H., et al., 2015. Dimerization of elongator protein 1 is essential for Elongator complex assembly. Proc. Natl. Acad. Sci. 112, 10697–10702.

Xu, P., et al., 2009. Quantitative proteomics reveals the function of unconventional ubiquitin chains in proteasomal degradation. Cell 137, 133–145.

Yamamoto, M., et al., 2003. Reversible suppression of glutamatergic neurotransmission of cerebellar granule cells in vivo by genetically manipulated expression of tetanus neurotoxin light chain. J. Neurosci. 23, 6759–6767.